

Revised stratigraphy and chronology for *Homo floresiensis* at Liang Bua in Indonesia

Thomas Sutikna^{1,2*}, Matthew W. Tocheri^{3,4*}, Michael J. Morwood^{1,‡}, E. Wahyu Saptomo^{1,2}, Jatmiko^{1,2}, Rokus Due Awe^{1,2,‡}, Sri Wasisto², Kira E. Westaway⁵, Maxime Aubert^{6,7}, Bo Li¹, Jian-xin Zhao⁸, Michael Storey⁹, Brent V. Alloway^{1,10}, Mike W. Morley¹, Hanneke J. M. Meijer^{4,11}, Gerrit D. van den Bergh¹, Rainer Grün^{12,13}, Anthony Dosseto¹⁴, Adam Brumm^{7,12}, William L. Jungers^{15,16} & Richard G. Roberts¹

Homo floresiensis, a primitive hominin species discovered in Late Pleistocene sediments at Liang Bua (Flores, Indonesia)^{1–3}, has generated wide interest and scientific debate. A major reason this taxon is controversial is because the *H. floresiensis*-bearing deposits, which include associated stone artefacts^{2–4} and remains of other extinct endemic fauna^{5,6}, were dated to between about 95 and 12 thousand calendar years (kyr) ago^{2,3,7}. These ages suggested that *H. floresiensis* survived until long after modern humans reached Australia by ~50 kyr ago^{8–10}. Here we report new stratigraphic and chronological evidence from Liang Bua that does not support the ages inferred previously for the *H. floresiensis* holotype (LB1), ~18 thousand calibrated radiocarbon years before present (kyr cal. BP), or the time of last appearance of this species (about 17 or 13–11 kyr cal. BP)^{1–3,7,11}. Instead, the skeletal remains of *H. floresiensis* and the deposits containing them are dated to between about 100 and 60 kyr ago, whereas stone artefacts attributable to this species range from about 190 to 50 kyr in age. Whether *H. floresiensis* survived after 50 kyr ago—potentially encountering modern humans on Flores or other hominins dispersing through southeast Asia, such as Denisovans^{12,13}—is an open question.

The 2001–2004 excavations at Liang Bua (Fig. 1) revealed the skeletal remains of *H. floresiensis*^{1–3,14–20} at 4–7 m depth in multiple excavated areas (referred to here as Sectors). Charcoal samples collected from similar depths near the eastern wall of the cave (Sector VII) were dated to between about 19 and 13–11 kyr cal. BP^{2,3,7}, whereas an age of ~74 kyr was obtained by coupled electron-spin resonance/uranium-series dating of a *Stegodon florensis insularis* molar recovered from ~4.5 m depth from near the cave centre (Sector IV)^{2,7}. This molar was found ~30 cm below a *H. floresiensis* premolar and ulna (LB2) and ~20 cm and ~130 cm above other postcranial remains (LB10 and LB3, respectively)¹⁸.

The 2007–2014 excavations between and slightly south of these Sectors (Fig. 1c) have revealed new stratigraphic details that are crucial for (re)interpreting the ages inferred originally for *H. floresiensis* (Extended Data Fig. 1 and Supplementary Video 1). The *H. floresiensis*-bearing deposits consist of multiple layers of fine-grained sediment interstratified by layers of weathered limestone, speleothem and loose gravel (Extended Data Fig. 2). These deposits are conformably overlain by an ~2-m-thick sequence of five tephras (referred to here as T1–T5;

Extended Data Fig. 3 and Supplementary Information section 1), separated by clastic sediments and flowstones (Fig. 2). This stratigraphic sequence forms a large pedestal that extends ~12 m laterally from the eastern wall to the cave centre, and is at least 6 m long from north to south. The pedestal is thickest (~4 m) in the middle rear of the cave, where it extends to within ~2 m of the present surface of the cave floor.

The pedestal deposits have been truncated by one or more phases of erosion, resulting in an erosional surface (that is, an unconformity) that slopes steeply down towards the cave mouth (Fig. 3 and Extended Data Figs 4 and 5). The specific timing and nature of the erosional events responsible for this unconformity remain unknown, but presumably include slope wash and other hydrogeological mechanisms, given the active karst setting of the cave. This unconformity was not recognized during the 2001–2004 excavations, raising serious questions about the accuracy of previous age estimates^{2,3,7} for *H. floresiensis*, which were based on inferred stratigraphic associations. To address these questions, we have applied several dating methods to the main stratigraphic units within this pedestal and to the skeletal remains of *H. floresiensis* and other fauna derived from this depositional sequence (see Supplementary Information sections 2–6 for details of each dating method).

Sediment samples for infrared stimulated luminescence (IRSL) and thermoluminescence (TL) dating^{21,22} (Extended Data Figs 6 and 7) were collected from the *H. floresiensis*-bearing deposits directly underlying T1 in the south baulks of Sectors XXI and XXIII, more than 2 m south of the erosional unconformity. These samples gave statistically indistinguishable weighted mean IRSL and TL ages ($\pm 1\sigma$) of 65 ± 5 kyr (LB12-OSL3 to -OSL6) and 71 ± 13 kyr (LB12-23-2 and -4), respectively, for the time since sand-sized grains of feldspar and quartz were last exposed to sunlight. A TL age of 89 ± 7 kyr (LB08-15-3) was obtained for the basal *H. floresiensis*-bearing deposits in Sector XV, while two further samples from the immediately underlying, gravel-rich layer (in Sectors XXI and XXIII) gave IRSL and TL ages of 128 ± 17 kyr (LB12-OSL7) and 113 ± 9 kyr (LB12-23-1), respectively. We also used ²³⁴U/²³⁰Th methods to date four samples of *in situ* speleothem from the *H. floresiensis*-bearing deposits in Sectors XII and XVII (LB07-SXII-F4 and LB09-SXVII-F1 to -F3), which gave ages ($\pm 2\sigma$) of between 80.8 ± 0.8 and 58.3 ± 0.5 kyr.

¹Centre for Archaeological Science, School of Earth and Environmental Sciences, University of Wollongong, Wollongong, New South Wales 2522, Australia. ²Pusat Penelitian Arkeologi Nasional, Jakarta 12510, Indonesia. ³Department of Anthropology, Lakehead University, Thunder Bay, Ontario P7B 5E1, Canada. ⁴Human Origins Program, Department of Anthropology, National Museum of Natural History, Smithsonian Institution, Washington DC 20013, USA. ⁵Traps MQ Luminescence Dating Facility, Department of Environmental Sciences, Macquarie University, Sydney, New South Wales 2109, Australia. ⁶Research Centre for Human Evolution, Place, Evolution and Rock Art Heritage Unit, Griffith University, Gold Coast, Queensland 4222, Australia. ⁷School of Earth and Environmental Sciences, University of Wollongong, Wollongong, New South Wales 2522, Australia. ⁸School of Earth Sciences, University of Queensland, Brisbane, Queensland 4072, Australia. ⁹QUADLAB, Section of Earth and Planetary System Science, Natural History Museum of Denmark, 1350 Copenhagen, Denmark. ¹⁰School of Geography, Environment and Earth Sciences, Victoria University of Wellington, Wellington 6012, New Zealand. ¹¹Department of Natural History, University Museum of Bergen, University of Bergen, 5007 Bergen, Norway. ¹²Research Centre for Human Evolution, Environmental Futures Research Institute, Griffith University, Brisbane, Queensland 4111, Australia. ¹³Research School of Earth Sciences, Australian National University, Canberra, Australian Capital Territory 0200, Australia. ¹⁴GeoQuEST Research Centre, School of Earth and Environmental Sciences, University of Wollongong, Wollongong, New South Wales 2522, Australia. ¹⁵Department of Anatomical Sciences, Stony Brook University Medical Center, Stony Brook, New York 11794, USA. ¹⁶Association Vahatra, BP 3972, Antananarivo 101, Madagascar.

*These authors contributed equally to this work.

‡Deceased.

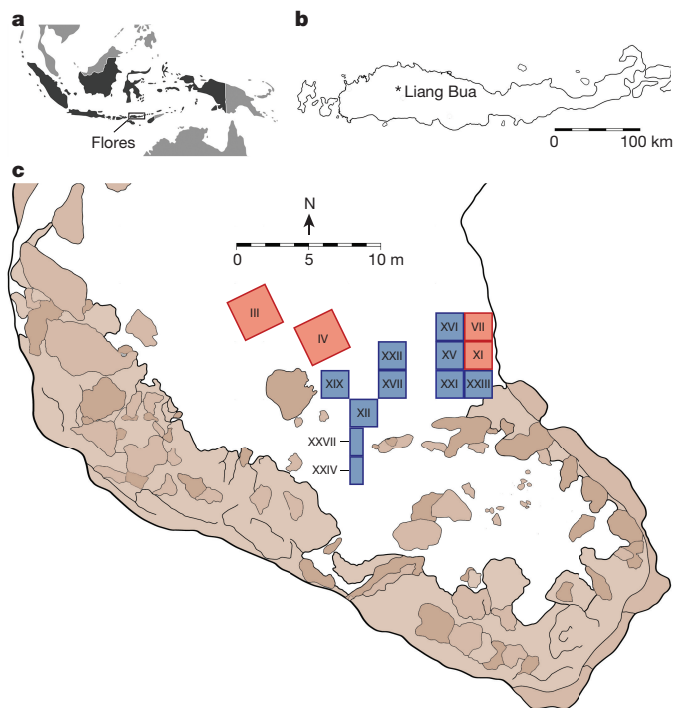


Figure 1 | Site location. **a**, Location of Flores within Indonesia. **b**, Location of Liang Bua on Flores. **c**, Site plan of Sectors discussed in the text (the 2001–2004 and 2007–2014 excavations are shaded red and blue, respectively). The remaining cave floor sediments are shaded white, while the areas shaded brown are exposed rocks, stalagmites and other surfaces covered in speleothems.

Three *H. floresiensis* ulnae and seven *Stegodon* bones were sampled for $^{234}\text{U}/^{230}\text{Th}$ dating, as well as a modern human femoral shaft fragment from the Holocene deposits in Sector IV (Extended Data Figs 8 and 9). Owing to the open system behaviour of bone, such analyses usually yield minimum ages for bone deposition and subsequent uranium uptake²³. The modelled age²⁴ of ~ 7.5 kyr for the modern human bone (132A/LB/IV/27D/03) is consistent with charcoal ^{14}C ages for the underlying and overlying sediments (~ 9.5 and 6.4 kyr cal. BP, respectively⁷). The *H. floresiensis* ulnae have modelled $^{234}\text{U}/^{230}\text{Th}$ ages ($\pm 2\sigma$) for individual laser-ablation tracks that range from 86.9 ± 7.9 to 71.5 ± 4.3 kyr for LB1 (Sectors VII and XI), 71.4 ± 1.1 to 66.7 ± 0.8 kyr for LB2 (Sector IV), and 66.0 ± 4.3 to 54.6 ± 2.1 kyr for LB6 (Sector XI). The *Stegodon* bone samples (all from Sector XI) span a modelled age range of 80.6 ± 11.3 to 40.5 ± 2.0 kyr, with the youngest minimum age deriving from a bone (U-s-05/LB/XI/51/04) recovered from the same sediments and depth as LB6. Delayed diffusion of uranium into the dense bone matrix of *Stegodon* may account for the youngest minimum ages appearing more recent than those obtained for the bones of *H. floresiensis*, the speleothems and the sediments.

We dated T1, which directly overlies the *H. floresiensis*-bearing deposits, using $^{40}\text{Ar}/^{39}\text{Ar}$ methods^{25,26}. The inverse isochron age ($\pm 1\sigma$) of 79 ± 12 kyr (Extended Data Fig. 3) is imprecise owing to the low yield of radiogenic argon from the hornblende crystals, but the 2σ age range (103 – 55 kyr) is consistent with the luminescence and $^{234}\text{U}/^{230}\text{Th}$ ages for the underlying samples. Immediately overlying T1 is a series of interstratified sedimentary units, including T2 and several flowstones. These are in turn overlain by T3, a ~ 0.75 m-thick volcanoclastic mass flow deposit, formerly referred to as the ‘black tuff’ or similar^{18,27}.

Sediments between T2 and T3 in Sector XXI yielded a weighted mean IRSL age of 66 ± 9 kyr (LB12-OSL1 and -OSL2) and a TL age of 59 ± 13 kyr (LB12-23-3). Interbedded flowstones and a small stalagmite in the same Sector gave $^{234}\text{U}/^{230}\text{Th}$ ages of between 66.1 ± 0.3 and 54.4 ± 0.3 kyr (LB-S.XXI 5 #08, LB-S.XXI 8-T #09 and 8-B #10, and LB/S.XXI 10-01 and -01R), while in Sector XII—nearer the cave

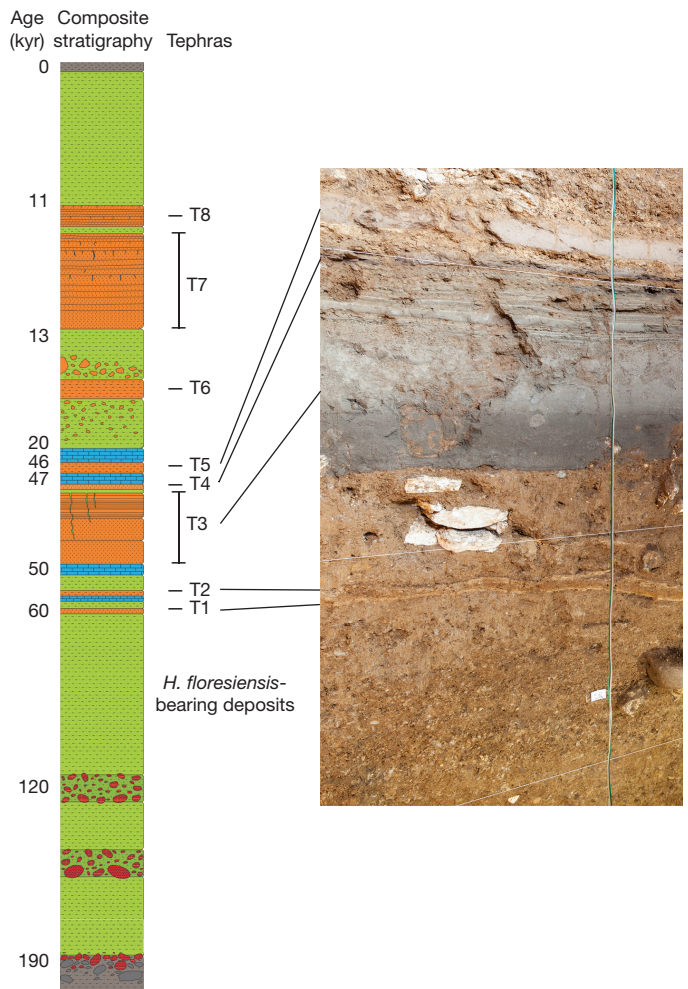


Figure 2 | Composite stratigraphic section of deposits at Liang Bua, with approximate ages. The deposits accumulated above a fluvial conglomerate and are capped by recent sediments (both shown in grey). Skeletal remains of *Homo floresiensis* occur in deposits stratigraphically beneath a sequence of eight volcanic tephras (T1–T8), separated by calcitic speleothems (blue) and fine-grained clastic sediments (green). As the thickness, grain size and slope angle of each unit vary considerably within the cave, only the approximate relative thicknesses of the units discussed in the text are shown; the minimum depth of this composite section would exceed 15 m. See Fig. 3 and Extended Data Fig. 5a for three-dimensional representations of the stratigraphy. Also indicated are units with concentrations of rounded, gravel-size clasts of igneous rock (red) or irregularly shaped, eroded fragments of T1, T2 and T3 (orange), and units with signs of bioturbation (upper parts of T3 and T7). The photograph shows T1–T5 and interstratified sediments that conformably overlie the *H. floresiensis*-bearing deposits (south baulk of Sector XXI).

centre—a flowstone immediately underlying T3 (LB07-SXII-F1) was dated to 49.6 ± 0.5 kyr. Hominin skeletal remains have not been recovered from the deposits between T2 and T3. However, stone artefacts are present and these display similar raw material proportions to those found underneath T1 ($\sim 80\%$ silicified tuff and $\sim 20\%$ chert), in contrast to the preference of modern humans for chert ($\sim 60\%$) observed at Liang Bua during the Holocene⁴. Also present in these sediments and those underlying T1 are the remains of other extinct large-bodied taxa, including *Stegodon*, giant marabou stork and vulture^{5,6}. The specific processes that ultimately resulted in the extinction of these taxa and *H. floresiensis* remain poorly understood.

Overlying T3 is T4, which is covered by loose, coarse gravel in two of the southernmost Sectors excavated (XII and XXVII). Three flowstone samples^{7,28} (weighted mean $^{234}\text{U}/^{230}\text{Th}$ age of 46.6 ± 0.5 kyr) directly overlie the southern parts of this coarse gravel layer. From the eastern

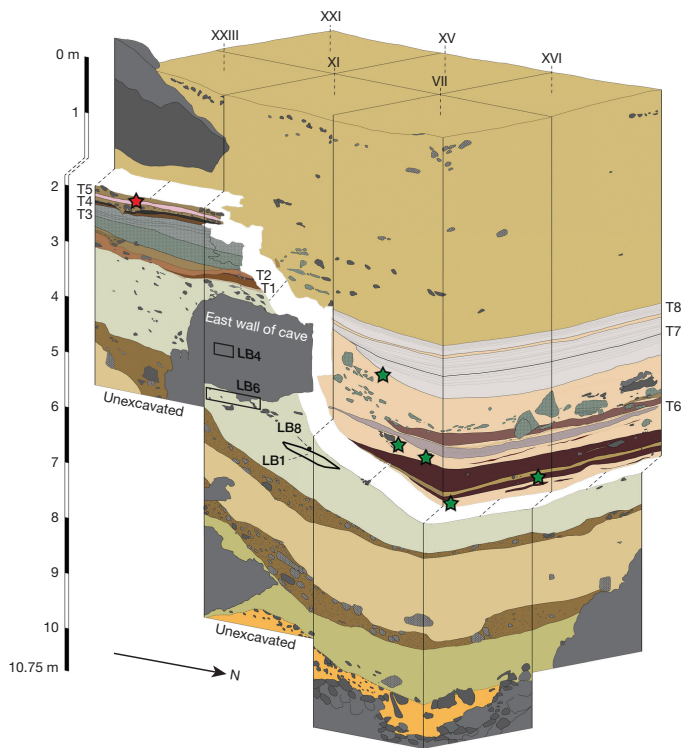


Figure 3 | Stratigraphy of excavated Sectors near the eastern wall of the cave. Multiple specimens of *Homo floresiensis* (LB1, LB4, LB6 and LB8) were recovered previously^{1–3,14–20} from sediments now recognized to directly underlie a sequence of five tephtras (T1–T5) and interstratified deposits. Together, these remnant deposits form a pedestal, the top of which is dated to ~46 kyr cal. BP (charcoal sample denoted by the red star at ~2 m depth in Sector XXIII). The overlying section—separated here by a white band and dotted lines for emphasis—represents deposits (including three additional tephtras, T6–T8) that rest unconformably on the steeply sloping erosional surface of the pedestal. The green stars in Sector VII mark the respective locations (from top to bottom) of the charcoal samples dated to approximately 13.0, 18.5, 18.1, 19.0 and 19.2 kyr cal. BP, which were used erroneously^{2,3,7} to infer the latest occurrences of *H. floresiensis*.

wall to the cave centre, T4 is overlain by two flowstone layers that are separated from each other by T5. At 1.89 m depth in Sector XXIII, charcoal (sample OxA-X-2648-13) from immediately above the upper surface of T5 yielded a ¹⁴C age of ~46 kyr cal. BP (95% confidence interval of 47.7–44.1 kyr cal. BP).

In contrast, all of the charcoal samples used previously to infer ages of ~18 kyr cal. BP for LB1 and about 17 or 13–11 kyr cal. BP as the *terminus ante quem* for *H. floresiensis* and *Stegodon*^{2,3,5,7} originate from deposits that unconformably overlie the remnant pedestal, based on their plotted coordinates (Fig. 3). These younger sediments are interstratified by three additional tephtras (T6–T8; Extended Data Fig. 10). Tephra T6 is observed at ~5.8 m depth in the northern parts of Sectors VII and XVI, followed by T7 and T8 (formerly referred to as the ‘white’ tuffaceous silts^{2,3,18,27}) at about 3.5–5 m depth (Sectors III, IV, VII, XI, XV, XVI and XXII). The onset of accumulation of the depositional sequence above the unconformity ~20 kyr ago is consistent with a TL age of 23 ± 7 kyr for sediments collected less than 15 cm above the unconformity in Sector XVI (LB09-16-2) and two new ¹⁴C ages of ~12.7 kyr cal. BP for charcoal recovered from just beneath T7 in Sector XXII (D-AMS 005953 and 005954).

Portions of the pedestal have been reworked into this younger depositional sequence. In Sector XXII, a displaced slab of intact pedestal deposit rests above the unconformity but underlies T7 (Extended Data Fig. 10c, d). In other Sectors, eroded fragments of T1, T2 and T3 are consistently observed in the younger, overlying deposits^{2,3,18}.

We investigated the possibility that the luminescence ages for the sediment samples collected in 2003 from alongside LB1 and ~1 m above it² were compromised by inadvertently sampling across the unconformity and measuring multiple grains simultaneously from this mixture. The wide spread in ages (from about 170 to 10 kyr ago) obtained for individual feldspar grains using newly developed IRSL dating procedures²¹ supports this suggestion (Extended Data Fig. 7k, l).

The new stratigraphic and chronological evidence for Liang Bua indicates that a pedestal of remnant deposits, dating to more than ~46 kyr cal. BP, has an erosional upper surface that slopes steeply downwards to the north and is unconformably overlain by sediments younger than ~20 kyr cal. BP. All skeletal remains assigned to *H. floresiensis* are from the pedestal deposits dated to approximately 100–60 kyr ago, while stone artefacts reasonably attributable to this species range from about 190 kyr²⁸ to 50 kyr in age. Parts of southeast Asia may have been inhabited by Denisovans^{12,13} or other hominins^{29,30} during this period, and modern humans had reached Australia by 50 kyr ago^{8–10}. But whether *H. floresiensis* survived after this time, or encountered modern humans, Denisovans or other hominin species on Flores or elsewhere, remain open questions that future discoveries may help to answer.

Online Content Methods, along with any additional Extended Data display items and Source Data, are available in the online version of the paper; references unique to these sections appear only in the online paper.

Received 31 August 2015; accepted 28 January 2016.

Published online 30 March 2016.

- Brown, P. *et al.* A new small-bodied hominin from the Late Pleistocene of Flores, Indonesia. *Nature* **431**, 1055–1061 (2004).
- Morwood, M. J. *et al.* Archaeology and age of a new hominin from Flores in eastern Indonesia. *Nature* **431**, 1087–1091 (2004).
- Morwood, M. J. *et al.* Further evidence for small-bodied hominins from the Late Pleistocene of Flores, Indonesia. *Nature* **437**, 1012–1017 (2005).
- Moore, M. W., Sutikna, T., Jatmiko, Morwood, M. J. & Brumm, A. Continuities in stone flaking technology at Liang Bua, Flores, Indonesia. *J. Hum. Evol.* **57**, 503–526 (2009).
- van den Bergh, G. D. *et al.* The Liang Bua faunal remains: a 95 kyr sequence from Flores, East Indonesia. *J. Hum. Evol.* **57**, 527–537 (2009).
- Meijer, H. J. M. *et al.* Late Pleistocene–Holocene non-passerine avifauna of Liang Bua (Flores, Indonesia). *J. Vertebr. Paleontol.* **33**, 877–894 (2013).
- Roberts, R. G. *et al.* Geochronology of cave deposits at Liang Bua and of adjacent river terraces in the Wae Racang valley, western Flores, Indonesia: a synthesis of age estimates for the type locality of *Homo floresiensis*. *J. Hum. Evol.* **57**, 484–502 (2009).
- Roberts, R. G. *et al.* Thermoluminescence dating of a 50,000-year-old human occupation site in northern Australia. *Nature* **345**, 153–156 (1990).
- Bowler, J. M. *et al.* New ages for human occupation and climatic change at Lake Mungo, Australia. *Nature* **421**, 837–840 (2003).
- Clarkson, C. *et al.* The archaeology, chronology and stratigraphy of Madjedbebe (Malakunanja II): a site in northern Australia with early occupation. *J. Hum. Evol.* **83**, 46–64 (2015).
- Morwood, M. J. *et al.* Preface: research at Liang Bua, Flores, Indonesia. *J. Hum. Evol.* **57**, 437–449 (2009).
- Reich, D. *et al.* Genetic history of an archaic hominin group from Denisova Cave in Siberia. *Nature* **468**, 1053–1060 (2010).
- Reich, D. *et al.* Denisova admixture and the first modern human dispersals into Southeast Asia and Oceania. *Am. J. Hum. Genet.* **89**, 516–528 (2011).
- Falk, D. *et al.* The brain of *Homo floresiensis*. *Science* **308**, 242–245 (2005).
- Larson, S. G. *et al.* *Homo floresiensis* and the evolution of the hominin shoulder. *J. Hum. Evol.* **53**, 718–731 (2007).
- Tocheri, M. W. *et al.* The primitive wrist of *Homo floresiensis* and its implications for hominin evolution. *Science* **317**, 1743–1745 (2007).
- Jungers, W. L. *et al.* The foot of *Homo floresiensis*. *Nature* **459**, 81–84 (2009).
- Morwood, M. J. & Jungers, W. L. (Eds). Paleoanthropological Research at Liang Bua, Flores, Indonesia. *J. Hum. Evol.* **57**, 437–648 (2009).
- Kaifu, Y. *et al.* Craniofacial morphology of *Homo floresiensis*: description, taxonomic affinities, and evolutionary implication. *J. Hum. Evol.* **61**, 644–682 (2011).
- Orr, C. M. *et al.* New wrist bones of *Homo floresiensis* from Liang Bua (Flores, Indonesia). *J. Hum. Evol.* **64**, 109–129 (2013).
- Li, B., Jacobs, Z., Roberts, R. G. & Li, S.-H. Review and assessment of the potential of post-IRSL dating methods to circumvent the problem of anomalous fading in feldspar luminescence. *Geochronometria* **41**, 178–201 (2014).
- Westaway, K. E. & Roberts, R. G. A dual-aliquot regenerative-dose protocol (DAP) for thermoluminescence (TL) dating of quartz sediments using the light-sensitive and isothermally stimulated red emissions. *Quat. Sci. Rev.* **25**, 2513–2528 (2006).

23. Grün, R., Eggers, S., Kinsley, L., Moseley, H. & Sambridge, M. Laser ablation U-series analysis of fossil bones and teeth. *Palaeogeogr. Palaeoclimatol. Palaeoecol.* **416**, 150–167 (2014).
24. Sambridge, M., Grün, R. & Eggers, S. U-series dating of bone in an open system: the diffusion-adsorption-decay model. *Quat. Geochronol.* **9**, 42–53 (2012).
25. Storey, M., Roberts, R. G. & Saidin, M. Astronomically calibrated $^{40}\text{Ar}/^{39}\text{Ar}$ age for the Toba supereruption and global synchronization of late Quaternary records. *Proc. Natl Acad. Sci. USA* **109**, 18684–18688 (2012).
26. Rivera, T. A., Storey, M., Schmitz, M. D. & Crowley, J. L. Age intercalibration of $^{40}\text{Ar}/^{39}\text{Ar}$ sanidine and chemically distinct U/Pb zircon populations from the Alder Creek Rhyolite Quaternary geochronology standard. *Chem. Geol.* **345**, 87–98 (2013).
27. Westaway, K. E. *et al.* *Homo floresiensis* and the late Pleistocene environments of eastern Indonesia: defining the nature of the relationship. *Quat. Sci. Rev.* **28**, 2897–2912 (2009).
28. Westaway, K. E. *et al.* Establishing the time of initial human occupation of Liang Bua, western Flores, Indonesia. *Quat. Geochronol.* **2**, 337–343 (2007).
29. Mijares, A. S. *et al.* New evidence for a 67,000-year-old human presence at Callao Cave, Luzon, Philippines. *J. Hum. Evol.* **59**, 123–132 (2010).
30. van den Bergh, G. D. *et al.* Earliest hominin occupation of Sulawesi, Indonesia. *Nature* **529**, 208–211 (2016).

Supplementary Information is available in the online version of the paper.

Acknowledgements The 2007–2014 excavations at Liang Bua were supported by an Australian Research Council (ARC) Discovery Project grant to M.J.M. (DP0770234), a Waitt Foundation/National Geographic Society grant to M.W.T. and T.S. (No. 2121-2) and a Smithsonian Scholarly Studies Program award to M.W.T. Additional funding was provided by the Peter Buck Fund for Human Origins Research, the Smithsonian's Human Origins Program, the University of

Wollongong (UOW) and the ARC (DP1093049 to K.E.W.). T.S. is supported by a UOW postgraduate scholarship, M.W.T. by a Canada Research Chair, M.A. and A.B. by ARC Discovery Early Career Researcher Awards (DE140100254 and DE130101560, respectively), B.L. by an ARC Future Fellowship (FT14010038), R.G.R. by an ARC Australian Laureate Fellowship (FL130100116) and B.V.A. by a Victoria University of Wellington Science Faculty Research Grant (201255). QUADLAB is funded by the Villum Foundation. Fieldwork was authorised by Pusat Penelitian Arkeologi Nasional (Jakarta, Indonesia) and Pemerintah Daerah Kabupaten Manggarai (Flores, Nusa Tenggara Timur). We also thank I Made Geria, V. N. Sene, R. Potts, P. Goldberg, K. Douka, G. Veatch, V. Rossi, A. Metallo, L. Kinsley, Y. Jafari, T. Lachlan, A. D. Nguyen, D. Yurnaldi, R. Setiawan, I Dewa Kompiang and the entire Liang Bua Team from Teras, Golo Manuk and Bere.

Author Contributions M.J.M., R. P. Soejono and R.G.R. conceived and coordinated the original research program at Liang Bua (2001–2004). The new excavations were planned and directed by T.S., E.W.S. and M.J.M. (2007–2009), and by T.S., M.W.T., E.W.S., J. and M.J.M. (2010–2014). T.S. led the stratigraphic analyses, with major contributions from M.W.T., S.W., M.J.M., K.E.W., R.D.A., E.W.S. and J., and additional input from M.W.M., H.J.M.M., G.D.vdB., B.V.A., A.B., W.L.J. and R.G.R. Dating analyses were conducted by B.L. and R.G.R. (IRSL), K.E.W. (TL), M.A., R.G. and A.D. ($^{234}\text{U}/^{230}\text{Th}$, bones), J.-x.Z. ($^{234}\text{U}/^{230}\text{Th}$, speleothems), and M.S. ($^{40}\text{Ar}/^{39}\text{Ar}$). B.V.A. analysed the volcanic tephra, R.D.A., H.J.M.M., G.D.vdB., M.W.T. and W.L.J. analysed the faunal remains, and J. analysed the stone artefacts. T.S., M.W.T. and R.G.R. wrote the paper, with early contributions from M.J.M. and additional input from all other authors.

Author Information Reprints and permissions information is available at www.nature.com/reprints. The authors declare no competing financial interests. Readers are welcome to comment on the online version of the paper. Correspondence and requests for materials should be addressed to T.S. (thomasutikna@gmail.com), M.W.T. (tocherim@gmail.com) and R.G.R. (rgrob@uow.edu.au).

METHODS

Archaeological excavation. The 2007–2014 excavations at Liang Bua, including eight 2×2 m and two 1×2 m areas (referred to as Sectors), proceeded in 10 cm intervals (referred to as spits) while following stratigraphic units. Timber shoring of the baulks was installed after ~ 2.5 m depth for safety. *In situ* findings (for example, bones, artefacts and charcoal) were plotted in three dimensions and the sediments from each spit were sieved by hand, followed by wet sieving (2 mm mesh). All recovered findings were cleaned, catalogued and transported to Pusat Penelitian Arkeologi Nasional (Jakarta, Indonesia) for curation and further study.

Electron microprobe analysis of volcanic glass. Bulk samples of four tephrae were wet sieved at $>32 \mu\text{m}$ and then dry sieved into $32\text{--}63 \mu\text{m}$, $63\text{--}125 \mu\text{m}$, $125\text{--}250 \mu\text{m}$, $250\text{--}500 \mu\text{m}$ and $500 \mu\text{m}\text{--}1$ mm fractions. Depending on the grain-size distribution of the sample, the dominant dry fraction containing the most glass material was mounted into an epoxy resin. Glass from bubble-wall shards or vesiculated pumice fragments was analysed as individual grains ($>63 \mu\text{m}$) using an electron microprobe. Major element determinations were made using a JEOL Superprobe (JXA-8230) housed at Victoria University of Wellington, New Zealand, using the ZAF correction method³¹. Analyses were performed with 15 kV accelerating voltage, 8 nA beam current, and an electron beam defocused to $10\text{--}20 \mu\text{m}$. Standardization was achieved by means of mineral and glass standards. Rhyolitic glass standard ATHO-G (ref. 32) was routinely used to monitor calibration in all analytical runs and to evaluate any day-to-day differences in calibration. All analyses were normalized to 100% (by weight) anhydrous and total iron was calculated as FeO (Supplementary Information section 1). The major element compositions of the four tephrae and the Youngest Toba Tuff³³ are displayed as bivariate plots in Extended Data Fig. 3c–e.

Infrared stimulated luminescence (IRSL) dating of feldspar grains. Sediment samples were collected using opaque plastic tubes hammered horizontally into cleaned stratigraphic sections and wrapped in black plastic after removal. Field measurements of the gamma dose rate at each sample location were made using a portable gamma-ray detector (Exploranium GR-320) inserted into the emptied tube holes. Sediment samples were also collected from the tube holes for laboratory determinations of water content and beta dose rate at the University of Wollongong. The environmental dose rate of each sample was calculated as the sum of the beta dose rate (estimated from beta-counting of dried and powdered sediment samples using a Riso low-level beta multicounter system and allowing for beta-dose attenuation and other factors³⁴), the *in situ* gamma dose rate, and the estimated cosmic-ray dose rate³⁵. The latter took account of the burial depth of each sample, the thickness of cave roof overhead, the zenith-angle dependence of cosmic rays, and the latitude, longitude and altitude of Liang Bua. Each of these external dose rate contributors were adjusted for long-term water content. The measured (field) water contents of the seven samples collected in 2012 range from 26 to 35%, but higher and lower field water contents have been reported for other sediment samples collected at Liang Bua: 15–30% (ref. 2), 3–22% (ref. 7) and 24–39% (Supplementary Information section 2). We used a value of $20 \pm 5\%$ as a mid-range estimate of the long-term water content, with the standard error sufficient to cover (at 2σ) most of the field measurements. The total dose rate of each sample also includes an estimate of the internal beta dose rate due to the radioactive decay of ^{40}K and ^{87}Rb . This estimate was based on a K concentration of $12 \pm 1\%$, determined from energy- and wavelength-dispersive X-ray spectroscopic measurements of individual feldspar grains^{36,37} (see Supplementary Information section 2), and an assumed Rb concentration of $400 \pm 100 \mu\text{g g}^{-1}$ (ref. 38). Potassium-rich feldspar (K-feldspar) grains of $90\text{--}212$ or $180\text{--}212 \mu\text{m}$ diameter were extracted from the sediment samples under dim red illumination and prepared using standard procedures³⁹, including the use of a sodium polytungstate solution of 2.58 g cm^{-3} density to separate the feldspar grains from heavier minerals. The separated grains were also washed in 10% hydrofluoric acid for 40 min to clean their surfaces and reduce the thickness of the alpha-irradiated outer layer by $\sim 15 \mu\text{m}$, which was taken into account in the dose rate calculation. For each sample, single aliquots composed of a few hundred grains were measured using an automated Riso TL/OSL reader equipped with infrared (875 nm) light-emitted diodes (LEDs) for stimulation⁴⁰ and a calibrated $^{90}\text{Sr}/^{90}\text{Y}$ source for beta irradiations. We also made measurements of individual K-feldspar grains ($180\text{--}212 \mu\text{m}$ diameter) from two samples collected in 2012 (LB12-OSL3 and -OSL4) and the two original sediment samples (LBS7-40a and LBS7-42a) collected from above and alongside the remains of LB1 (ref. 2). Infrared stimulation of individual K-feldspar grains was achieved using a focused laser beam (830 nm)⁴⁰. The IRSL emissions from the single aliquots and single grains were detected using an Electron Tubes Ltd 9235B photomultiplier tube fitted with Schott BG-39 and Corning 7-59 filters to transmit wavelengths of $320\text{--}480 \text{ nm}$. To estimate the equivalent dose (D_e) for each aliquot or grain^{39,41}, we initially used the multiple elevated temperature post-infrared IRSL (MET-pIRIR) regenerative-dose procedure^{21,30,42}, in which the IRSL signals are measured by

progressively increasing the stimulation temperature from 50°C to 250°C in 50°C increments. The samples yielded very dim signals, however, so we used a two-step pIRIR procedure^{21,43} to improve the signal-to-noise ratio. Grains were preheated at 320°C for 60 s before infrared stimulation of the natural, regenerative and test doses at 50°C for 200 s. The pIRIR signal was then measured at 290°C for either 200 s (single aliquots) or 1 s (single grains), followed by an infrared bleach at 325°C for 100 s at the end of each regenerative-dose cycle. Example pIRIR decay and dose-response curves are shown in Extended Data Fig. 7a–c. Performance tests of the regenerative-dose procedure and details of residual dose measurements^{21,44} and anomalous fading tests^{45,46} are described in Supplementary Information section 2. We estimated the pIRIR age of each sample from the weighted mean D_e (calculated using the central age model^{47,48}) divided by the environmental dose rate, and applied corrections for residual dose and anomalous fading. For the latter corrections, we used the weighted mean fading rate ($0.9 \pm 0.3\%$ per decade) measured for five of the seven samples collected in 2012.

Thermoluminescence (TL) dating of quartz grains. Sediment samples were taken in the same manner as the IRSL samples, as were the *in situ* gamma dose rate measurements (made using an ORTEC digi-DART gamma-ray detector). Additional sediment samples were also collected for determinations of water content and beta dose rate at Macquarie University. The environmental dose rate of each sample consists of three external components, each adjusted for long-term water content ($20 \pm 5\%$): the beta dose rate (estimated from beta-counting and allowing for beta-dose attenuation), the *in situ* gamma dose rate, and the estimated cosmic-ray dose rate. An assumed internal dose rate of $0.03 \pm 0.01 \text{ Gy kyr}^{-1}$ was also included in the total dose rate. Quartz grains were separated from the sediment samples under dim red illumination and prepared using standard procedures³⁹, including mineral separations using 2.70 and 2.62 g cm^{-3} density solutions of sodium polytungstate to isolate the quartz and a 40% hydrofluoric acid etch for 45 min to remove the alpha-irradiated outer $\sim 20 \mu\text{m}$ of each grain. Aliquots composed of about 10,000 quartz grains were measured using a dual-aliquot regenerative-dose TL protocol²² to isolate the light-sensitive red emissions⁴⁹. This procedure was originally developed for application at Liang Bua² and requires two aliquots of each sample: one to estimate the D_e associated with the heat-reset TL traps and the other to measure the total TL signal, from which the D_e associated with the light-sensitive TL traps is estimated by subtraction. Measurements were made on a Riso TL/OSL reader fitted with an Electron Tubes Ltd 9658B photomultiplier tube and Schott BG-39 and Kopp 2-63 filters designed to transmit red emissions (peak transmission in the $600\text{--}620 \text{ nm}$ range, with minimum and maximum wavelengths of 580 and 670 nm), and cooled to -22°C to reduce the background count rate. Bleaching was performed using a halogen lamp and light guide integrated into the reader, and laboratory doses were given using a $^{90}\text{Sr}/^{90}\text{Y}$ source mounted on the reader. The quartz grains were first heated to 260°C at a heating rate of 5 K s^{-1} and then held at this temperature for 1,000 s to induce an isothermal TL signal and reduce the unwanted glow from incandescence. Following ref. 22, D_e values were estimated from the 20–30 s interval of isothermal TL (which was shown to be light-sensitive) and the final 160 s was used as background. Two of the samples contained abundant quantities of quartz, so problems associated with inter-aliquot variability^{50,51} were reduced by measuring 12 replicates of each pair of aliquots (Supplementary Information section 2). As prolonged sunlight exposure is required the empty the light-sensitive TL traps, the ages obtained should be regarded as maximum estimates of the time elapsed since sediment deposition²².

Uranium-series ($^{234}\text{U}/^{230}\text{Th}$) dating of bones. Samples of bone from three specimens of *Homo floresiensis* (LB1, LB2 and LB6), one *Homo sapiens* and eight *Stegodon florensis insularis* were analysed using laser ablation uranium-series isotope measurement analysis procedures and instruments similar to those described previously^{23,52}. Cuts were made perpendicular to the bone surface using a rotatory tool equipped with a thin ($100 \mu\text{m}$ wide) diamond saw blade. The cut samples were mounted into aluminium cups, aligning the cross-sectioned surfaces with the outer rim of the sample holder to position the samples on the focal plane of the laser in the sampling cell. Sequential laser spot analyses were undertaken along 1–5 parallel tracks per sample, starting from the interior of each cross-sectioned bone (Extended Data Figs 8 and 9 and Supplementary Information section 3). Uranium and thorium isotopes were measured at the Australian National University using a Finnigan MAT Neptune multi-collector inductively-coupled plasma mass spectrometer (MC-ICP-MS) equipped with multiple Faraday cups and ion counters. Two ion counters were set to masses of 230.1 and 234.1, while the Faraday cups measured the masses 232, 235 and 238. Samples were ablated using a Lambda Physik LPFPro ArF excimer laser (193 nm) coupled to the MC-ICP-MS through a custom-designed Helix ablation cell. The analyses were made at regular spacing (typically 2–3 mm) along each track, using a laser spot size of $265 \mu\text{m}$ and a 5 Hz pulse rate. The samples were initially cleaned for 5 s and ablation pits were measured for 50 s. These measurements were bracketed by analyses of reference

standards to correct for instrument drift. Semi-quantitative estimates of uranium and thorium concentrations were made from repeated measurements of the SRM NIST-610 glass standard (U: $461.5 \mu\text{g g}^{-1}$, Th: $457.2 \mu\text{g g}^{-1}$) and uranium-isotope (activity) ratios from repeated measurements of rhinoceros tooth dentine from Hexian sample 1118 (ref. 53). Apparent $^{234}\text{U}/^{230}\text{Th}$ ages were estimated for each track using a diffusion–adsorption–decay (DAD) model²⁴, which uses the entire set of isotope measurements made along the track to calculate the rate of diffusion of ^{238}U and ^{234}U into the bone. Bones behave as geochemically ‘open’ systems, so the diffusion of uranium into a bone may have occurred soon after it was deposited or much later. The original isotopic signature may also be overprinted by secondary uranium uptake that is hard to recognize. As such, uranium-series ages for bones are most likely to be minimum estimates of time since deposition, with the extent of age underestimation being very difficult or impossible to evaluate²³. The modelled ages were calculated after rejecting data points associated with detrital contamination (U/Th elemental ratios of ≤ 300) and data points at the surface of the bones where secondary overprinting was suspected. Results are tabulated in Supplementary Information section 3, with all errors given at 2σ .

Uranium-series ($^{234}\text{U}/^{230}\text{Th}$) dating of speleothems. Samples of calcite deposited as speleothems (flowstones and a 1 cm-tall stalagmite) were collected during excavation. Unlike bone, speleothems commonly behave as geochemically ‘closed’ systems, with no loss or gain of uranium after calcite crystallization⁵⁴. The cleanest portion of each sample was selected, ground to the size of a rice grain, cleaned ultrasonically and then handpicked, avoiding pieces that appeared to be porous or contaminated. Age determinations were made at the University of Queensland using a Nu Plasma MC-ICP-MS. Uranium and thorium separation procedures, MC-ICP-MS analytical protocols, details of spike calibrations, blank and ‘memory’ assessments, and repeat measurements of standards have been described previously^{55,56}. The $^{234}\text{U}/^{230}\text{Th}$ ages were calculated using Isoplot 3.75 (ref. 57) and half-lives of 245.25 kyr (^{234}U) and 75.69 kyr (^{230}Th) (ref. 58). As most samples consist of impure calcite with some degree of detrital contamination, a correction for non-radiogenic ^{230}Th was applied to the measured $^{230}\text{Th}/^{232}\text{Th}$ activity ratio of each sample using an assumed bulk-Earth $^{230}\text{Th}/^{232}\text{Th}$ activity ratio of 0.825 (with a relative error of $\pm 50\%$ and assuming secular equilibrium in the ^{238}U – ^{234}U – ^{230}Th decay chain), as is typical of most other studies⁵⁹. This non-radiogenic ^{230}Th correction reduces the calculated ages of the samples and increases the age uncertainties by an amount dependent on the extent of detrital contamination. All ten dated samples have measured $^{230}\text{Th}/^{232}\text{Th}$ activity ratios of >20 (Supplementary Information section 4), so the detritally-corrected $^{234}\text{U}/^{230}\text{Th}$ ages are only slightly younger than the uncorrected (measured) ages.

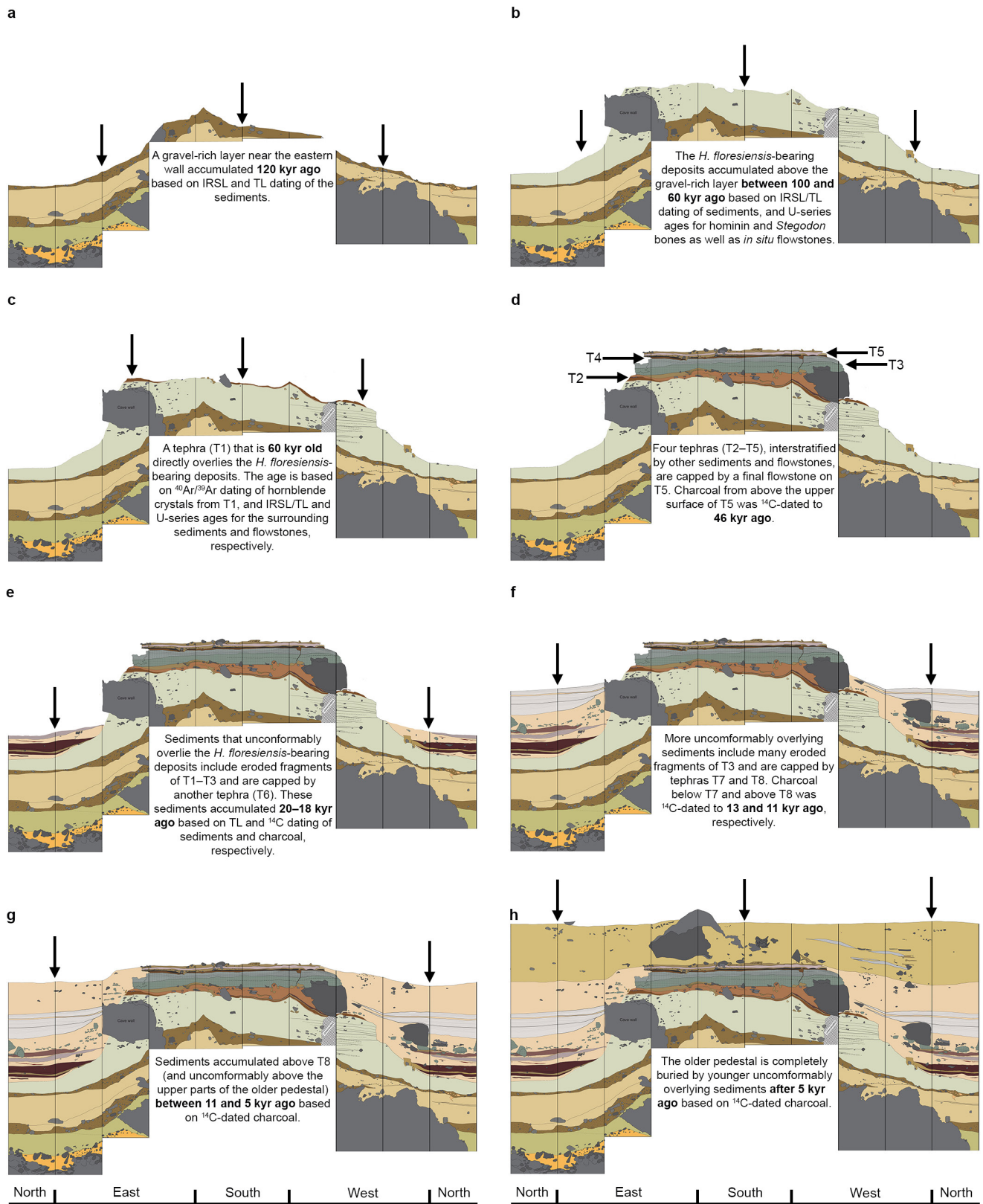
Argon–argon ($^{40}\text{Ar}/^{39}\text{Ar}$) dating of hornblende crystals. Crystals of hornblende were obtained for the 100–150 and 150–250 μm size fractions of the T1 tephra using standard heavy liquid and magnetic separation techniques. Crystals were loaded into wells in 18 mm-diameter aluminium sample discs for neutron irradiation, along with the 1.185 million year-old Alder Creek sanidine²⁶ as the neutron fluence monitor. Neutron irradiation was carried out for 4 min in the cadmium-shielded CLICIT facility at the Oregon State University TRIGA reactor. Argon isotopic analyses of gas released from 6 hornblende aliquots during CO_2 laser step-heating, including a final fusion step (‘fuse’ in Supplementary Information section 5), were made on a fully automated, high-resolution, Nu Instruments Noblesse multi-collector noble-gas mass spectrometer, using procedures documented previously²⁵. One set of four experiments (Lab IDs 2598 and 2599 in Supplementary Information section 5) consisted of strong degassing of 10 mg hornblende aliquots in square pits in the laser disc, using a beam integrator lens that gives a ‘top hat’ 6×6 mm energy profile at the focal plane. The laser was then operated at 32 W and this high-temperature, pre-fusion step measured (‘D’ in Supplementary Information section 5). The fusion step was performed using a conventional focus lens. In the second set of experiments, 20 mg hornblende aliquots were loaded into 5 mm-wide channels in the laser disc and a defocused laser beam was programmed to raster in 50 traverses, each 30 mm in length and separated by 0.1 mm. Low power (<1 W) steps were performed initially to remove loosely trapped argon. At 1 W of laser power (step ‘C’), the hornblende crystals began to glow and release significant amounts of ^{39}Ar . This and subsequent steps, including the final fusion, are reported in Supplementary Information section 5 as Lab IDs 2584-03C to -03O (fuse) and 2584-04C to -04I (fuse). Sample gas clean-up was through an all-metal extraction line, equipped with a -130°C cold trap (to remove H_2O) and two water-cooled SAES GP-50 getter pumps (to absorb reactive gases). Argon isotopic analyses of unknowns, blanks and monitor minerals were carried out in identical fashion during a fixed period of 400 s in 14 data acquisition cycles. ^{40}Ar and ^{39}Ar were measured on the high-mass ion counter, ^{38}Ar and ^{37}Ar on the axial ion counter and ^{36}Ar on the low-mass ion counter, with baselines measured every third cycle. Measurement of the ^{40}Ar , ^{38}Ar and ^{36}Ar ion beams was carried out simultaneously, followed by sequential measurement of ^{39}Ar and ^{37}Ar . Beam

switching was achieved by varying the field of the mass spectrometer magnet and with minor adjustment of the quad lenses. Data acquisition and reduction was performed using the program ‘Mass Spec’ (A. Deino, Berkeley Geochronology Center). Detector intercalibration and mass fractionation corrections were made using the weighted mean of a time series of measured atmospheric argon aliquots delivered from a calibrated air pipette²⁵. The accuracy of the primary air pipette measurements was verified by cross-referencing to data produced from a newly charged second air pipette. Decay and other constants, including correction factors for interference isotopes produced by nucleogenic reactions, are as reported in ref. 25. An isotope correlation (inverse isochron) plot of the data for all 28 aliquots is shown in Extended Data Fig. 3f. The age determined from the inverse isochron is 85 ± 13 kyr for all 28 aliquots, or 79 ± 12 kyr (errors at 1σ) if the data point on the far right-hand side of the plot is excluded. In both cases, the $^{40}\text{Ar}/^{36}\text{Ar}$ intercept value is statistically indistinguishable from the atmospheric ratio of 298.6 ± 0.3 (ref. 60), indicating the absence of significant excess ^{40}Ar in the hornblende crystals.

Radiocarbon (^{14}C) dating of charcoal. Three charcoal samples recovered during excavation were sent to DirectAMS Radiocarbon Dating Service in Bothell, Washington (Supplementary Information section 6). Samples were pretreated using acid–base–acid (ABA) procedures and the ^{14}C content was measured using accelerator mass spectrometry⁶¹. Conventional ^{14}C ages in radiocarbon years before present (BP) were converted to calendar-year age ranges at the 68% and 95% confidence intervals using the SHCal13 calibration data set⁶² and CALIB 7.1 (<http://calib.qub.ac.uk/calib/>). One of these three samples yielded an ‘old’ radiocarbon age (>40 kyr BP), so we submitted the remaining charcoal to the Oxford Radiocarbon Accelerator Unit (ORAU) for a harsher cleaning protocol known as ABOx-SC^{63,64}. This pretreatment is known to improve charcoal decontamination and has been shown repeatedly to produce more reliable results for ‘old’ charcoal. However, the harshness of the ABOx-SC procedure often results in large material loss and sample failure, so a new preparative method (AOx-SC) has been developed and tested at the ORAU (K. Douka, personal communication). The AOx-SC procedure does not include a NaOH step and produces identical results to ABOx-SC, but with much higher yields and reduced sample failure. For the Liang Bua sample, ~ 100 mg and ~ 50 mg of hand-picked charcoal underwent ABOx-SC and AOx-SC pretreatments, respectively. Only the AOx-treated charcoal survived the wet chemistry, yielding sufficient carbon for stepped combustion, first at 630°C and then at $1,000^\circ\text{C}$, with the latter fraction collected for graphitization and measurement by accelerator mass spectrometry.

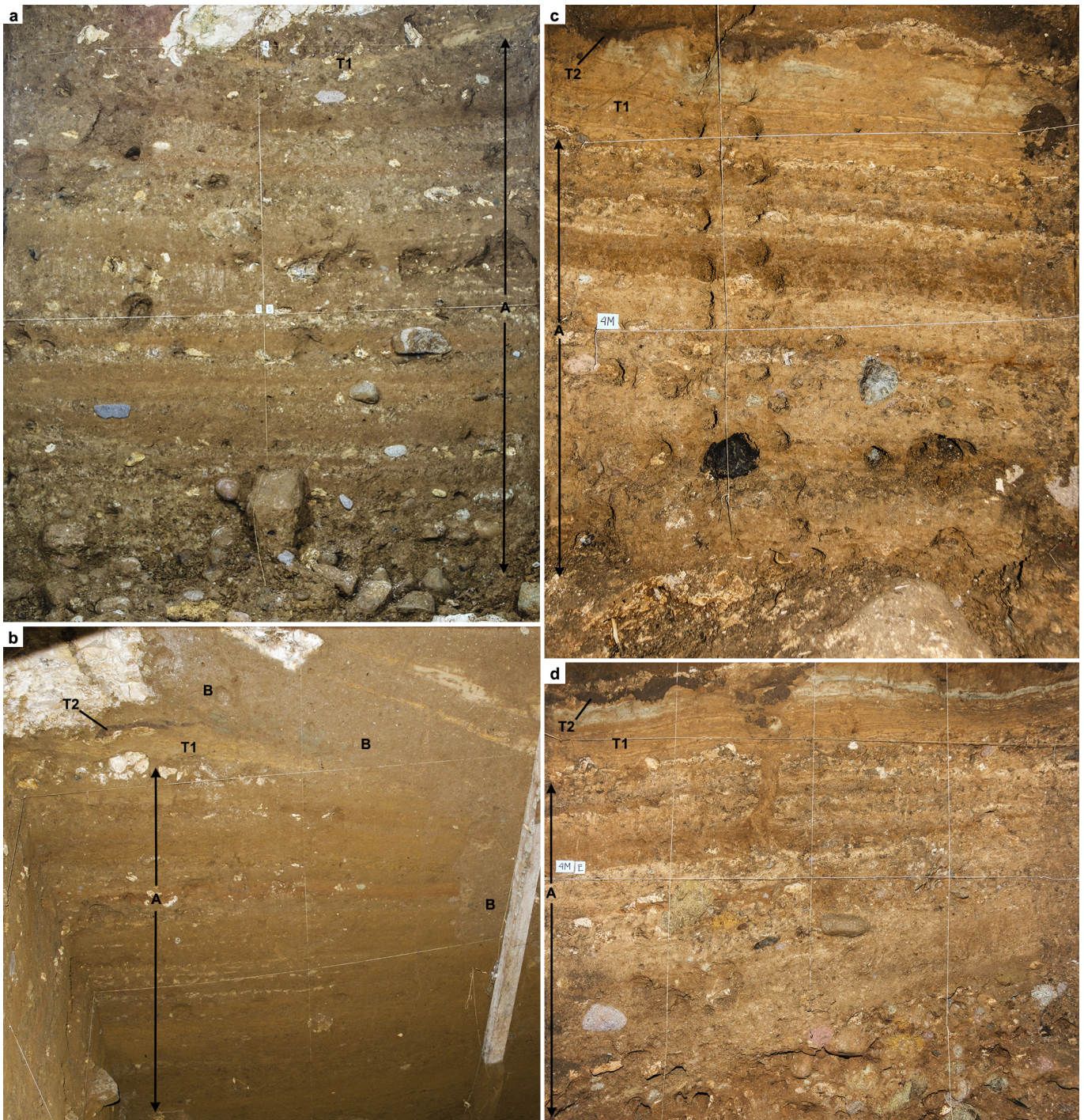
- Heinrich, K. F. J. in *Electron Probe Quantitation* (eds Heinrich, K. F. J. & Newbury, D. E.), 9–18 (Plenum, 1991).
- Jochum, K. P. et al. MPI-DING reference glasses for in situ microanalysis: New reference values for element concentrations and isotope ratios. *Geochim. Geophys. Geosyst.* **7**, Q02008 (2006).
- Alloway, B. V. et al. Correspondence between glass-FT and ^{14}C ages of silicic pyroclastic flow deposits sourced from Maninjau Caldera, west-central Sumatra. *Earth Planet. Sci. Lett.* **227**, 121–133 (2004).
- Jacobs, Z. & Roberts, R. G. An improved single grain OSL chronology for the sedimentary deposits from Diepkloof Rockshelter, Western Cape, South Africa. *J. Archaeol. Sci.* **63**, 175–192 (2015).
- Prescott, J. R. & Hutton, J. T. Cosmic ray contributions to dose rates for luminescence and ESR dating: large depths and long-term time variations. *Radiat. Meas.* **23**, 497–500 (1994).
- Neudorf, C. M., Roberts, R. G. & Jacobs, Z. Sources of overdispersion in a K-rich feldspar sample from north-central India: insights from D_{90} , K content and IRSL age distributions for individual grains. *Radiat. Meas.* **47**, 696–702 (2012).
- Neudorf, C. M. *Luminescence Investigations into the Time of Final Deposition of Toba Volcanic Ash and Artefact-bearing Alluvial Sediments in the Middle Son Valley, Madhya Pradesh, India*. PhD thesis, Univ. of Wollongong (2012).
- Huntley, D. J. & Hancock, R. G. V. The Rb contents of the K-feldspars being measured in optical dating. *Anc. TL* **19**, 43–46 (2001).
- Aitken, M. J. *An Introduction to Optical Dating* (Oxford Univ. Press, 1998).
- Bøtter-Jensen, L., Andersen, C. E., Duller, G. A. T. & Murray, A. S. Developments in radiation, stimulation and observation facilities in luminescence measurements. *Radiat. Meas.* **37**, 535–541 (2003).
- Roberts, R. G. et al. Optical dating in archaeology: thirty years in retrospect and grand challenges for the future. *J. Archaeol. Sci.* **56**, 41–60 (2015).
- Li, B. & Li, S.-H. Luminescence dating of K-feldspar from sediments: a protocol without anomalous fading correction. *Quat. Geochronol.* **6**, 468–479 (2011).
- Thiel, C. et al. Luminescence dating of the Stratzing loess profile (Austria) – testing the potential of an elevated temperature post-IRSL protocol. *Quat. Int.* **234**, 23–31 (2011).
- Li, B., Roberts, R. G. & Jacobs, Z. On the dose dependency of the bleachable and non-bleachable components of IRSL from K-feldspar: improved procedures for luminescence dating of Quaternary sediments. *Quat. Geochronol.* **17**, 1–13 (2013).
- Huntley, D. J. & Lamothe, M. Ubiquity of anomalous fading in K-feldspars and the measurement and correction for it in optical dating. *Can. J. Earth Sci.* **38**, 1093–1106 (2001).

46. Auclair, M., Lamothe, M. & Huot, S. Measurement of anomalous fading for feldspar IRSL using SAR. *Radiat. Meas.* **37**, 487–492 (2003).
47. Galbraith, R. F., Roberts, R. G., Laslett, G. M., Yoshida, H. & Olley, J. M. Optical dating of single and multiple grains of quartz from Jinmium rock shelter, northern Australia: Part 1, experimental design and statistical models. *Archaeometry* **41**, 339–364 (1999).
48. Galbraith, R. F. & Roberts, R. G. Statistical aspects of equivalent dose and error calculation and display in OSL dating: an overview and some recommendations. *Quat. Geochronol.* **11**, 1–27 (2012).
49. Franklin, A. D., Prescott, J. R. & Robertson, G. B. Comparison of blue and red TL from quartz. *Radiat. Meas.* **32**, 633–639 (2000).
50. Westaway, K. E. The red, white and blue of quartz luminescence: a comparison of D_e values derived for sediments from Australia and Indonesia using TL and OSL emissions. *Radiat. Meas.* **44**, 462–466 (2009).
51. Demeter, F. *et al.* Anatomically modern human in Southeast Asia (Laos) by 46 ka. *Proc. Natl Acad. Sci. USA* **109**, 14375–14380 (2012).
52. Eggins, S. M. *et al.* *In situ* U-series dating by laser-ablation multi-collector ICPMS: new prospects for Quaternary geochronology. *Quat. Sci. Rev.* **24**, 2523–2538 (2005).
53. Grün, R. *et al.* ESR and U-series analyses of teeth from the palaeoanthropological site of Hexian, Anhui Province, China. *J. Hum. Evol.* **34**, 555–564 (1998).
54. Hellstrom, J. & Pickering, R. Recent advances and future prospects of the U–Th and U–Pb chronometers applicable to archaeology. *J. Archaeol. Sci.* **56**, 32–40 (2015).
55. Zhou, H.-y., Zhao, J.-x., Wang, Q., Feng, Y.-x. & Tang, J. Speleothem-derived Asian summer monsoon variations in Central China, 54–46 ka. *J. Quat. Sci.* **26**, 781–790 (2011).
56. Clark, T. R. *et al.* Discerning the timing and cause of historical mortality events in modern *Porites* from the Great Barrier Reef. *Geochim. Cosmochim. Acta* **138**, 57–80 (2014).
57. Ludwig, K. R. *User's Manual for Isoplot 3.75: a Geochronological Toolkit for Microsoft Excel* (Berkeley Geochron. Center, 2012).
58. Cheng, H. *et al.* The half-lives of uranium-234 and thorium-230. *Chem. Geol.* **169**, 17–33 (2000).
59. Zhao, J.-x., Yu, K.-f. & Feng, Y.-x. High-precision ^{238}U – ^{234}U – ^{230}Th disequilibrium dating of the recent past: a review. *Quat. Geochronol.* **4**, 423–433 (2009).
60. Lee, J.-Y. *et al.* A redetermination of the isotopic abundances of atmospheric Ar. *Geochim. Cosmochim. Acta* **70**, 4507–4512 (2006).
61. Wood, R. From revolution to convention: the past, present and future of radiocarbon dating. *J. Archaeol. Sci.* **56**, 61–72 (2015).
62. Hogg, A. G. *et al.* SHCal13 Southern Hemisphere calibration, 0–50,000 years cal BP. *Radiocarbon* **55**, 1889–1903 (2013).
63. Bird, M. I. *et al.* Radiocarbon dating of “old” charcoal using a wet oxidation, stepped-combustion procedure. *Radiocarbon* **41**, 127–140 (1999).
64. Brock, F., Higham, T. F. G., Ditchfield, P. & Bronk Ramsey, C. Current pretreatment methods for AMS radiocarbon dating at the Oxford Radiocarbon Accelerator Unit (ORAU). *Radiocarbon* **52**, 103–112 (2010).



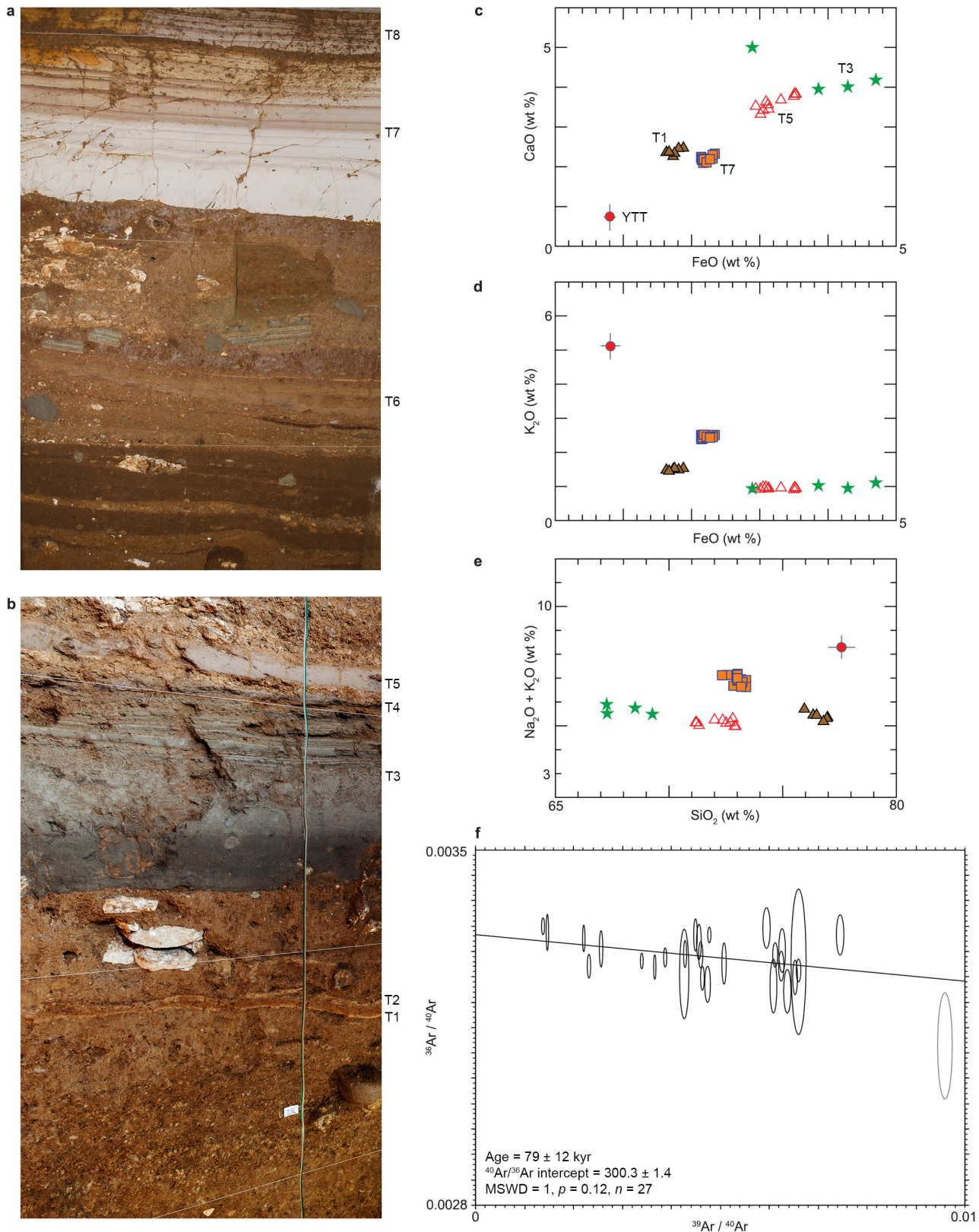
Extended Data Figure 1 | Stratigraphy of the excavated area near the eastern cave wall at eight stages of depositional history, with approximate ages indicated. a–h, Each panel shows the remnant deposits exposed in the 2-m-wide baulks of the following Sectors (from left to right): north VII, east VII, XI and XXIII, south XXIII and XXI, west XXI, XV and XVI, and north XVI. The pedestal deposits shown in b–d were

truncated by one or more phases of erosion that resulted in an erosional surface (that is, an unconformity) that slopes steeply down towards the cave mouth (see also Supplementary Video 1). The black arrows relate to the accompanying text in each panel. The maximum depth excavated was 10.75 m in Sector VII (for example, the left two panels in h).



Extended Data Figure 2 | Deposits containing the remains of *Homo floresiensis*. These deposits (A) consist of multiple layers of fine-grained sediment interspersed with layers of weathered limestone and loose gravel, and are directly overlain by two tephras (T1 and T2). **a**, South baulk of

Sector XV, near the eastern cave wall. **b**, West baulk of Sector XV, also showing the unconformably overlying deposits (B). **c**, **d**, North and east baulks of Sector XIX, near the cave centre.



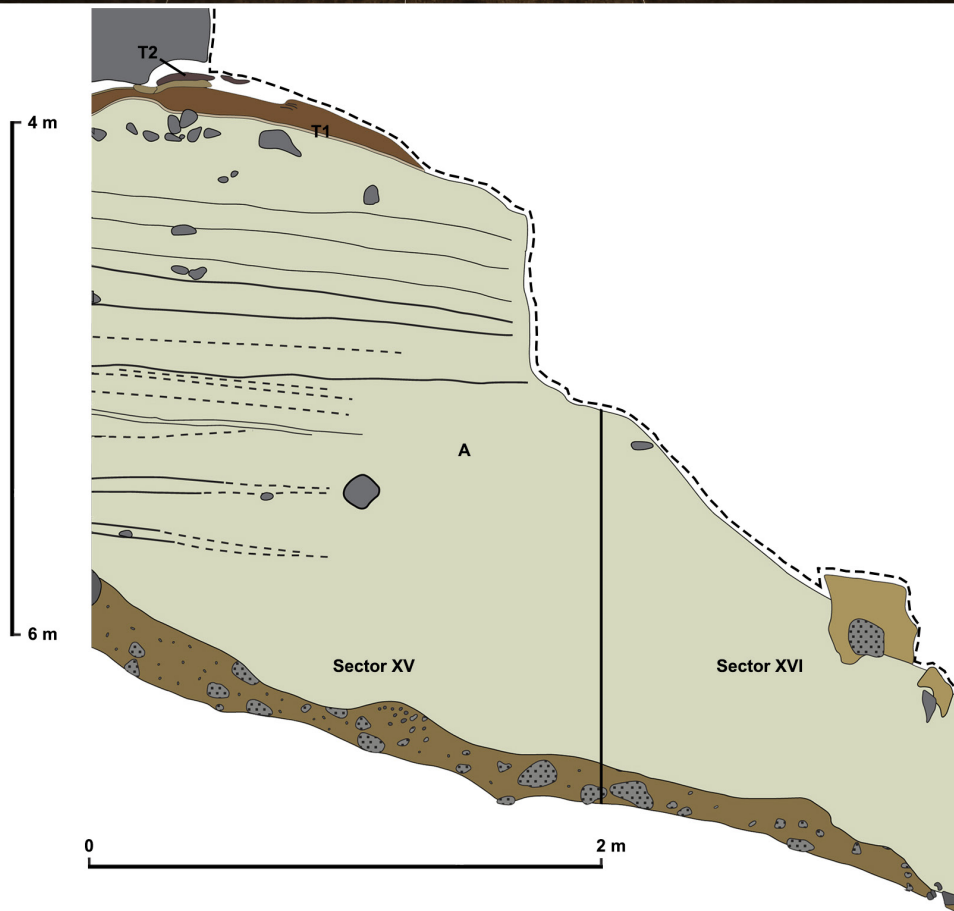
Extended Data Figure 3 | The volcaniclastic deposits at Liang Bua.

a, Photograph of tephras T6–T8 (north bank of Sector XVI). **b**, Photograph of tephras T1–T5 (south bank of Sector XXI). **c**, Bivariate plot of FeO and CaO concentrations (expressed as weight %), acquired by electron microprobe analysis of glass shards from T1 ($n = 6$), T3 ($n = 4$), T5 ($n = 10$) and T7 ($n = 15$), as well as the Youngest Toba Tuff (YTT, $n = 207, \pm 1\sigma$)

from northern Sumatra. **d**, Bivariate plot of FeO and K₂O concentrations (symbols as in **c**). **e**, Bivariate plot of SiO₂ and Na₂O + K₂O concentrations (symbols as in **c**). **f**, Isotope correlation (inverse isochron) plot for hornblende crystals from T1. The error ellipses represent individual analyses ($n = 28$). The ellipse on the far right-hand side was omitted from the $^{40}\text{Ar}/^{39}\text{Ar}$ age determination of 79 ± 12 kyr (at 1σ).



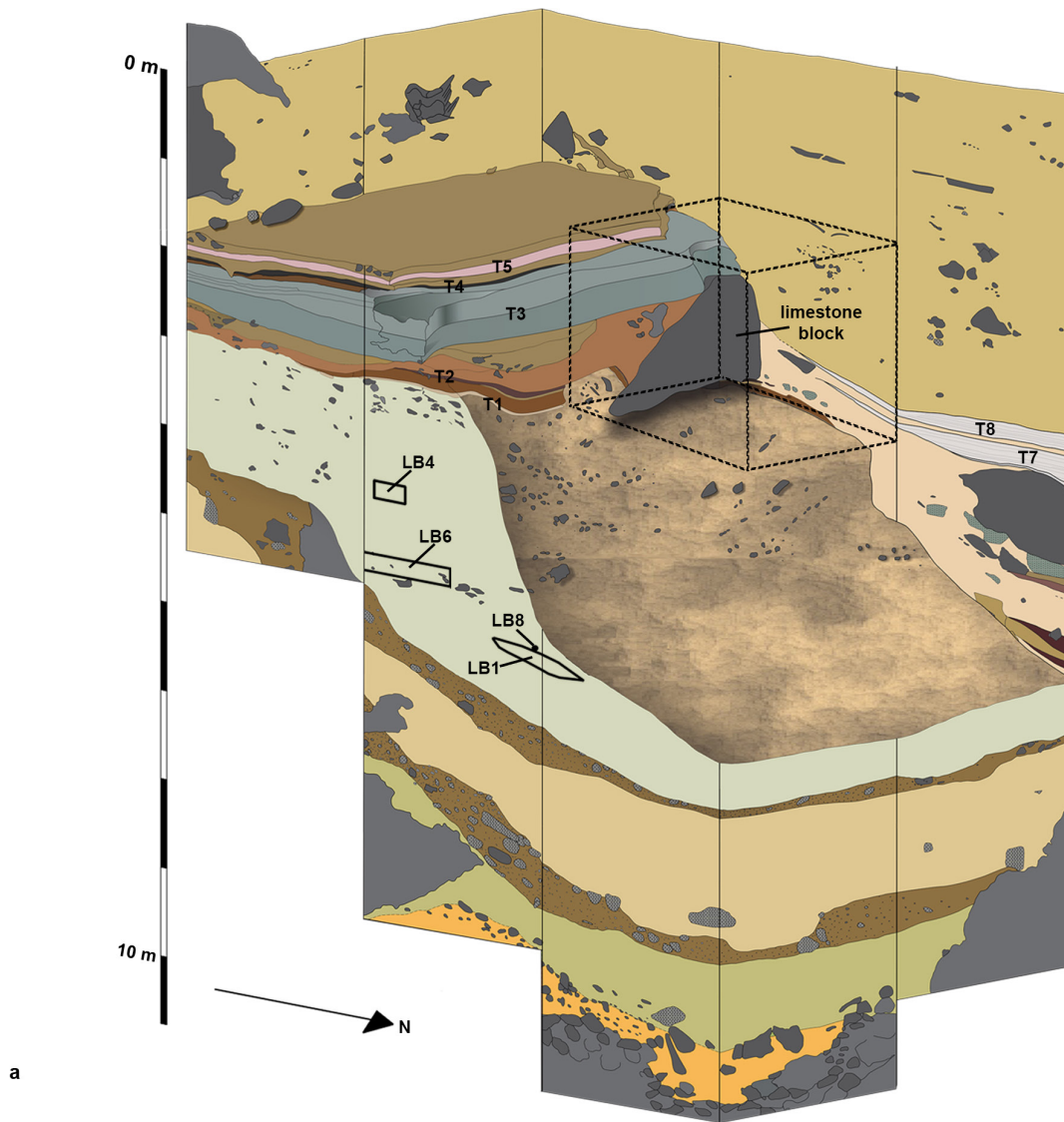
a



b

Extended Data Figure 4 | Erosional surface of the pedestal in the west baulks of Sectors XV and XVI. The dashed line marks the steeply sloping boundary between remnant deposits (T2, T1 and the underlying *Homo floresiensis*-bearing sediments) that comprise part of the pedestal (A)

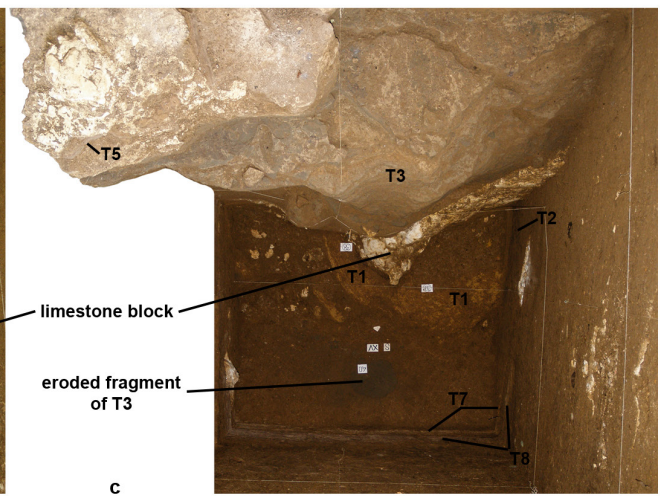
and the much younger deposits (B) that unconformably overlie the contact. **a**, Photograph taken at an upward angle showing the sedimentary differences between the deposits above and below the erosional boundary. **b**, Illustration of the erosional surface and underlying deposits shown in **a**.



a



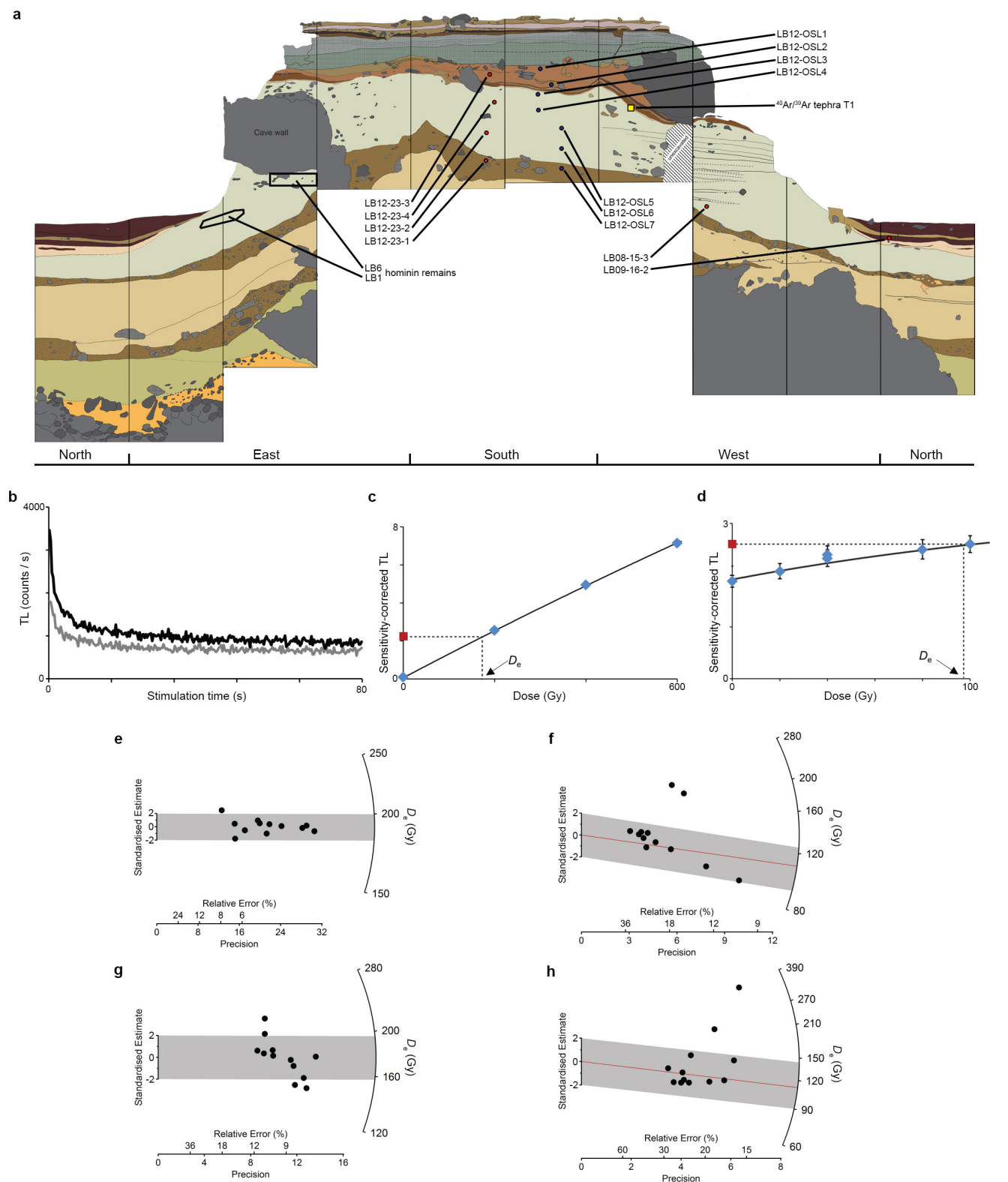
b



c

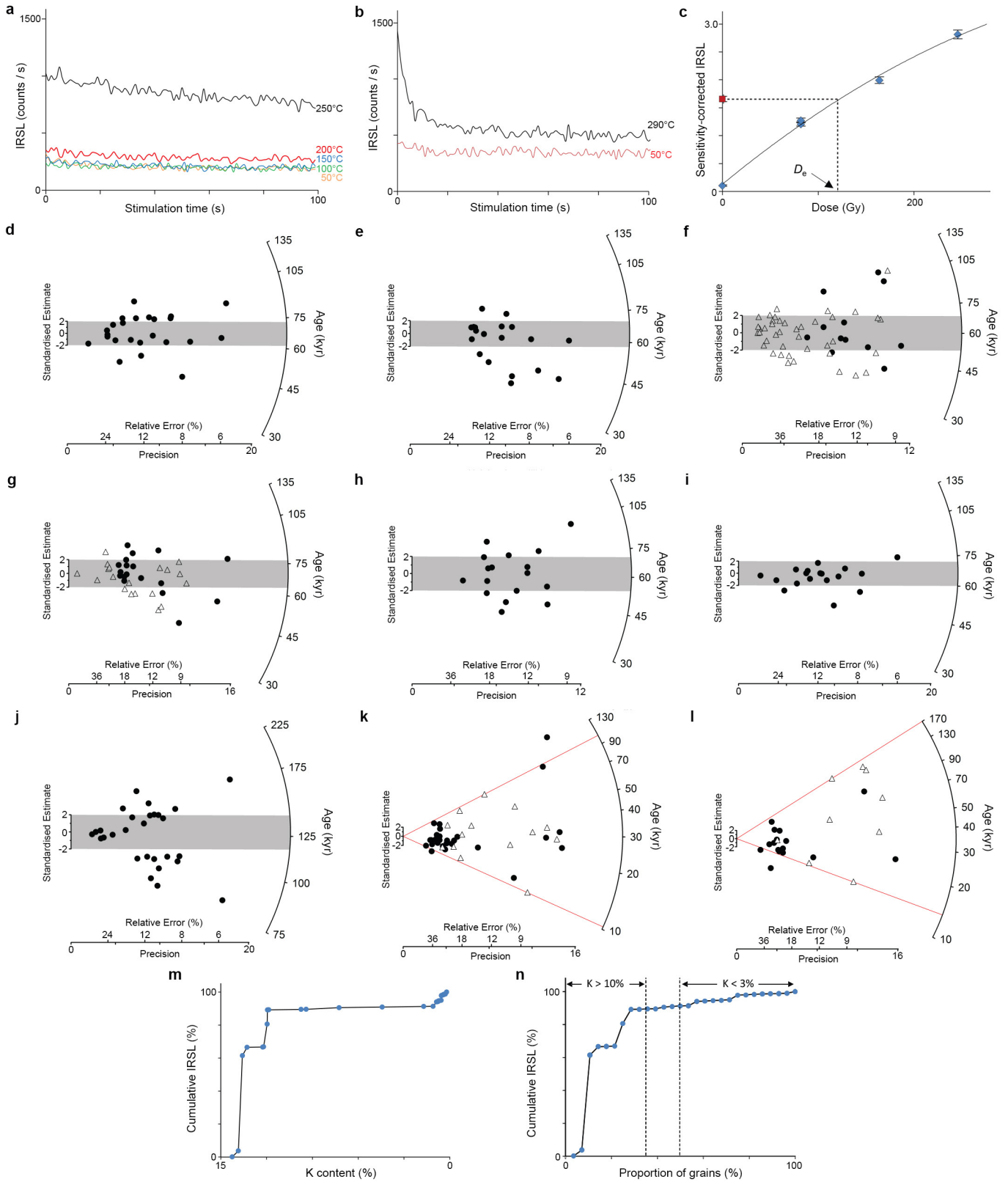
Extended Data Figure 5 | Erosional surface of the pedestal near the eastern wall of the cave. a, Illustration of the erosional surface and the locations of LB1, LB4, LB6 and LB8 below the boundary (see also Fig. 3). The deposits that unconformably overlie the pedestal are shown in the

south and west baulks. The stippled cube outlines the photographed area (in Sector XV) shown in b and c. Both photographs taken from above, with north towards the bottom of the page.



Extended Data Figure 6 | Locations of sediment samples dated in this study and TL data for quartz grains from Liang Bua. **a**, Stratigraphy of the excavated area near the eastern cave wall (Sector baulks as in Extended Data Fig. 1) with TL samples indicated by red circles, IRSL samples by blue circles and the $^{40}\text{Ar}/^{39}\text{Ar}$ sample by a yellow square. Also shown are the TL and IRSL sample codes and the locations of hominin remains LB1 and LB6. **b**, Representative isothermal (260 °C) TL decay curves for the natural (black line) and test dose (grey line) signals from sample LB08-15-3. **c**, **d**, Regenerated TL dose–response curves for one pair of Aliquots A and B of sample LB08-15-3, respectively; the equivalent dose (D_e) is estimated by

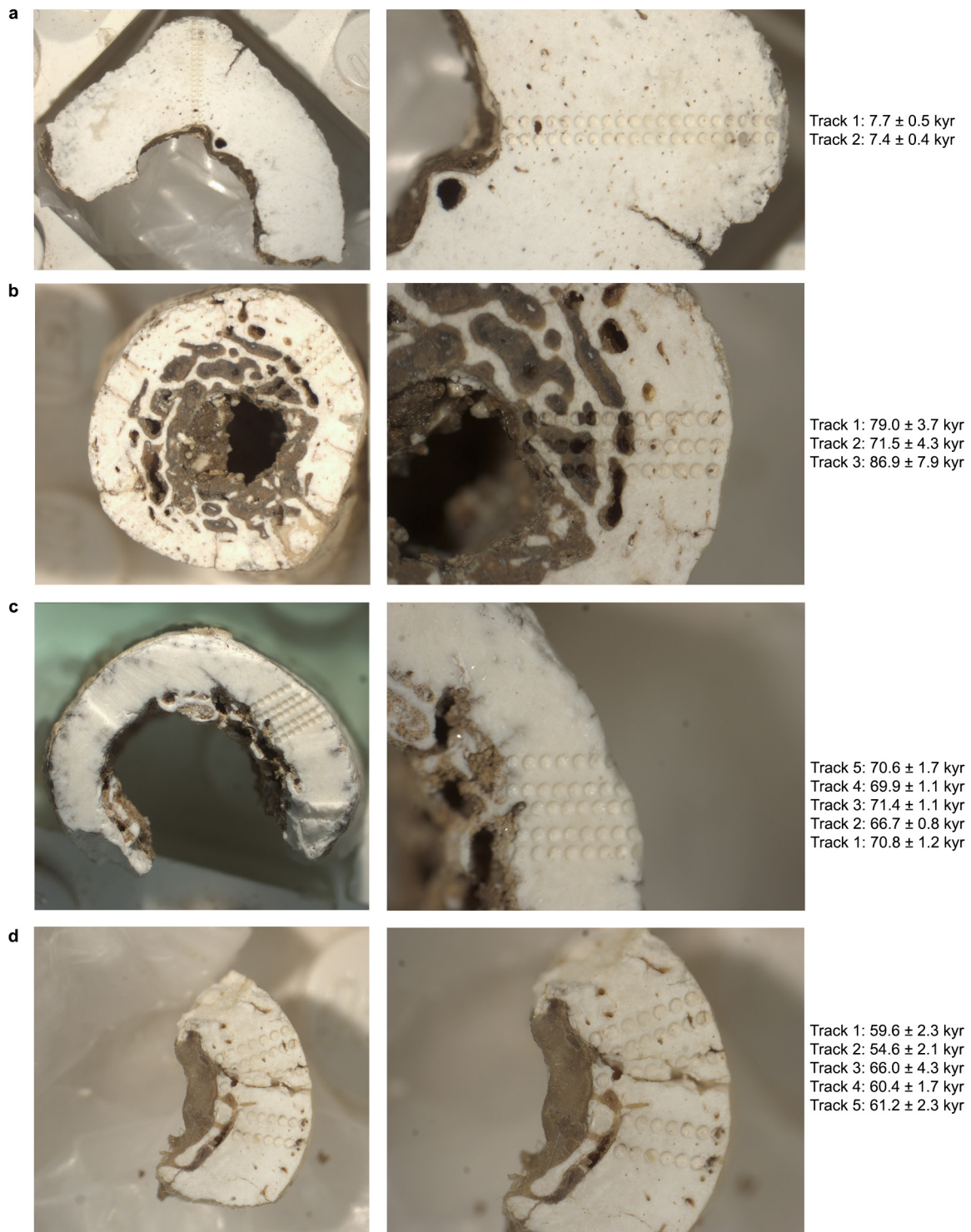
projecting the natural signal (red square) on to the dose–response curve fitted to the regenerated signals (blue diamonds). **e**, Radial plot^{47,48} of D_e values for Aliquot A ($n = 12$) of sample LB08-15-3; the grey band is centred on the weighted mean D_e calculated using the central age model. **f**, Radial plot of the corresponding D_e values for Aliquot B ($n = 12$) of the same sample. The grey band is centred on the central age model estimate, with the two high- D_e outliers omitted. The red line intersects the right-hand axis at the D_e calculated by fitting the minimum age model^{47,48} to all 12 values. **g**, **h**, Radial plots of D_e values for Aliquots A and B of sample LB12-23-1 (symbols as in **e** and **f**).



Extended Data Figure 7 | See next page for caption.

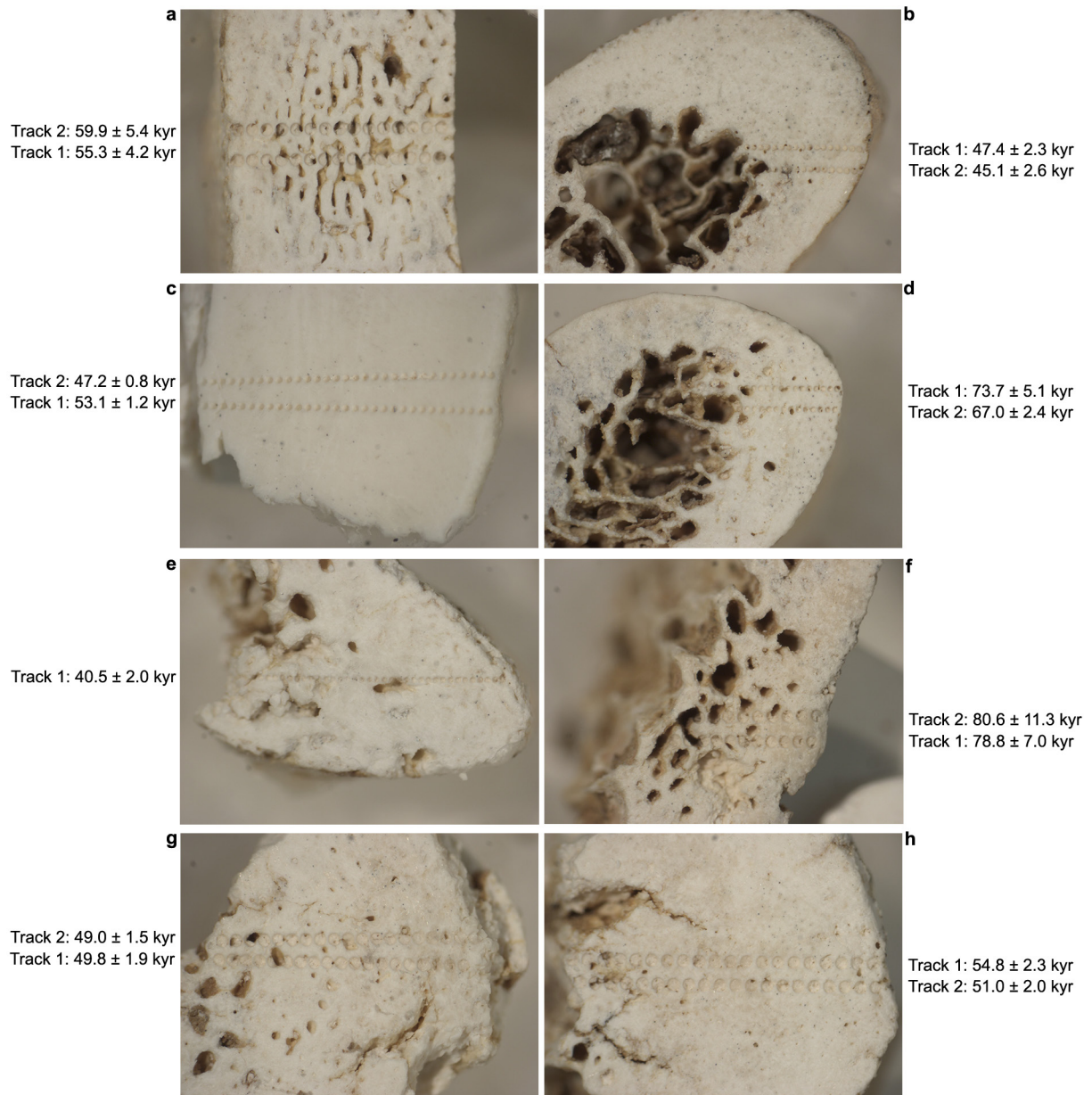
Extended Data Figure 7 | IRSL data and potassium (K) concentrations for feldspar grains from Liang Bua. **a**, Representative IRSL (50 °C) and multiple elevated temperature (100–250 °C) post-infrared IRSL (pIRIR) decay curves for a single aliquot of sample LB12-OSL1. **b**, IRSL (50 °C) and pIRIR (290 °C) decay curves for a different aliquot of LB12-OSL1. **c**, Regenerated pIRIR (290 °C) dose–response curve for the aliquot shown in **b**; the equivalent dose (D_e) is estimated by projecting the natural signal (red square) on to the dose–response curve fitted to the regenerated signals (blue diamonds). **d–j**, Radial plots of IRSL ages (corrected for residual dose and anomalous fading) for single aliquots of each sample: **d**, LB12-OSL1; **e**, LB12-OSL2; **f**, LB12-OSL3; **g**, LB12-OSL4; **h**, LB12-OSL5; **i**, LB12-OSL6; and **j**, LB12-OSL7. IRSL ages were also obtained for single grains of samples LB12-OSL3 and LB12-OSL4, and are shown as open triangles in **f** and **g**. The grey bands in each plot are centred on the

weighted mean ages calculated using the central age model. **k**, **l**, Radial plots of IRSL ages (corrected as for **d–j**) for samples LBS7-40a and LBS7-42a, respectively; single aliquots are shown as filled circles and single grains as open triangles. The upper and lower red lines intersect the right-hand axis at the maximum and minimum single-grain ages, respectively. **m**, Distribution of pIRIR intensities from 28 individual grains of feldspar from sample LB12-OSL3 that had been given a regenerative dose of 80 Gy. The relative contribution of each grain to the total (cumulative) pIRIR light sum is plotted as a function of K concentration (measured by wavelength-dispersive X-ray spectroscopy); note the reversed scale on the x -axis. **n**, Cumulative pIRIR light sum for the same 28 grains as shown in **m**, plotted as a function of grains ranked by K concentration (which decreases from left to right).



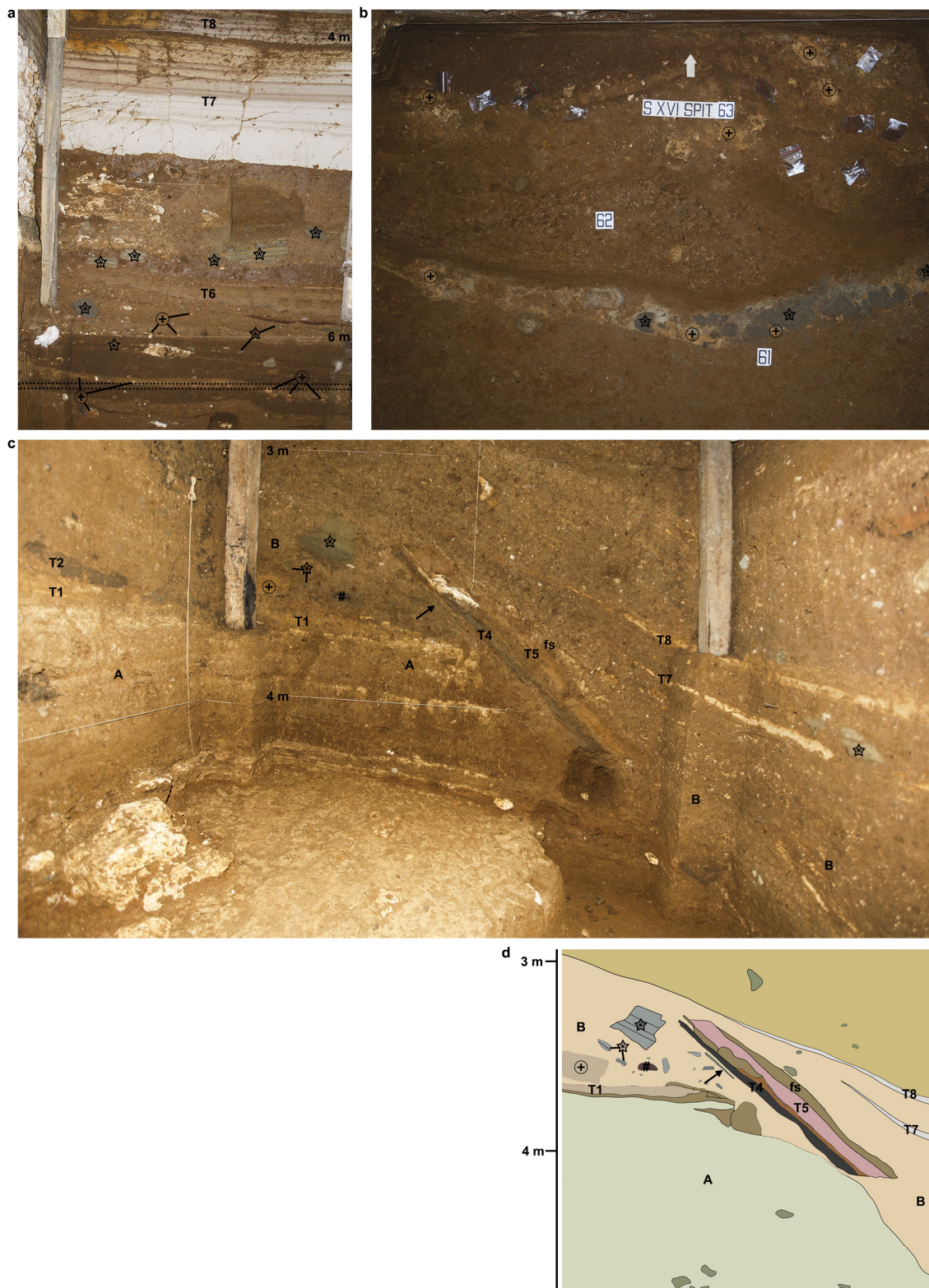
Extended Data Figure 8 | Laser-ablation uranium-series analyses of hominin bone fragments from various Sectors and spits (depth intervals), and their modelled ages. a, Modern human femur (132A/LB/27D/03) from Sector IV, spit 27 (265–275 cm). b, *Homo floresiensis*

ulna (LB1/52) from Sector XI, spit 58A (575–585 cm). c, *H. floresiensis* ulna (LB2/1) from Sector IV, spit 42D (415–425 cm). d, *H. floresiensis* ulna (LB6/3) from Sector XI, spit 51 (505–515 cm). Each laser spot is $265 \mu\text{m}$ in diameter and the age errors are at 2σ .



Extended Data Figure 9 | Laser-ablation uranium-series analyses of bone fragments of *Stegodon florensis insularis* from various spits (depth intervals) in Sector XI, and their modelled ages. a, U-s-01/LB/XI/32/04, spit 32 (315–325 cm). b, U-s-02/LB/XI/45/04, spit 45 (445–455 cm). c, U-s-03/LB/XI/47/04, spit 47 (465–475 cm). d, U-s-04/LB/XI/49/04,

spit 49 (485–495 cm). e, U-s-05/LB/XI/51/04, spit 51 (505–515 cm). f, U-s-06/LB/XI/52/04, spit 52 (515–525 cm). g, U-s-07/LB/XI/65/04, spit 65 (645–655 cm). h, U-s-08/LB/XI/65B/04, spit 65B (645–655 cm). Each laser spot is $265 \mu\text{m}$ in diameter and the age errors are at 2σ .



Extended Data Figure 10 | Deposits stratigraphically above the unconformity in Sector XVI and displaced slab of deposit in Sector XXII. **a**, The north baulk (~2 m wide) of Sector XVI. **b**, Excavated floors (white arrow points north) of spits 61–63 (615–635 cm depth); the field of view is ~1.6 m in width. The stippled box in **a** indicates the floor of spit 63 in **b**, where fragments of T1 (+) are visible in spit 63, and fragments of T3 (*) and T1 are concentrated in the band just above the label for spit 61. Eroded fragments (between about 1 cm and 60 cm in size) of T1, T2 and T3 have been consistently recovered from deposits unconformably overlying the erosional surface of the pedestal, indicating reworking of the pedestal deposits before ~13 kyr cal. BP. **c**, Photograph of the west baulk

and parts of the south and north baulks (at left and right, respectively) of Sector XXII showing a displaced slab of deposit that contains intact portions of the uppermost part of T3 (arrow) and the overlying layers, up to and including the flowstone (fs) that caps T5. The stratigraphic position of the slab beneath T7 and T8 indicates that it broke away from its original location, slightly to the south, and slid down the steeply sloping erosional surface before ~13 kyr cal. BP. Also shown are the *Homo floresiensis*-bearing deposits (A) and the unconformably overlying deposits (B), which include eroded fragments of T1 (+), T2 (#) and T3 (*). **d**, Illustration of the west baulk of Sector XXII, as shown in **c**.